Projectile fragmentation reactions and production of nuclei near the neutron drip line

M. Notani,[1,*] H. Sakurai,[2,†] N. Aoi,[3] H. Iwasaki,[2,‡] N. Fukuda,[3] Z. Liu,[3,§] K. Yoneda,[3] H. Ogawa,[3] T. Teranishi,[1,‖] T. Nakamura,[4] H. Okuno,[3] A. Yoshida,[3] Y. X. Watanabe,[3,¶] S. Momota,[5] N. Inabe,[3] T. Kubo,[3] S. Ito,[3] A. Ozawa,[3,**] T. Suzuki,[3,††] I. Tanihata,[3,‡‡] and M. Ishihara[3]

[1]*Center for Nuclear Study, University of Tokyo (CNS) RIKEN Campus, 2-1 Hirosawa, Wako, Saitama 351-0198, Japan*

[2]*Department of Physics, University of Tokyo, 7-3-1 Hongo, Bunkyo, Tokyo 113-0033, Japan*

[3]*RIKEN Nishina Center, 2-1 Hirosawa, Wako, Saitama 351-0198, Japan*

[4]*Department of Applied Physics, Tokyo Institute of Technology, 2-12-1 Oh-okayama, Meguro-ku, Tokyo 152-8551, Japan*

[5]*Department of Intelligent Mechanical Systems Engineering, Kochi University of Technology, Tosayamada-cho, Kochi 782, Japan*

(Received 22 February 2007; published 16 October 2007)

The reaction mechanism of projectile fragmentation at intermediate energies has been investigated by observing the target dependence of the production cross sections of very neutron rich nuclei. Measurement of longitudinal momentum distributions of projectile-like fragments in a broad range of fragment mass and charge was performed using a 100 MeV/nucleon ^{40}Ar beam incident on Be and Ta targets. By measurement of the fragment momentum distribution, a parabolic mass dependence of the momentum peak shift was observed in the results of both targets, and light-fragment acceleration was found only in the Be-target data. The analysis of production cross sections revealed an obvious enhancement of the target dependence except for a target size effect when the neutron excess is increased. This result implies the breakdown of factorization of production cross sections for very neutron rich nuclei near the drip line.

DOI: 10.1103/PhysRevC.76.044605 PACS number(s): 25.70.Mn, 27.20.+n, 27.30.+t

I. INTRODUCTION

During the past two decades, unstable nuclei have become an important object of study in nuclear physics. Nuclear fragmentation of heavy-ion beams is utilized for producing secondary beams of unstable nuclei far from β-stability. For designing experiments with secondary beams, a good knowledge of production cross sections is essential. To deduce the production cross sections efficiently, an empirical parametrization of fragmentation cross sections (EPAX) is widely used in simulation programs for projectile-fragment separators [1–3]. For reaction mechanisms, fragmentation models based on the abrasion-ablation scheme (AA models) are often applied to estimate the production cross sections.

With the recent development of heavy-ion accelerators, the number of accessible nuclei lying far from the β-stability line has been increasing. An example has been shown by the experimental findings of particle stability of ^{31}F [4], ^{31,34}Ne [5,6], ^{37}Na [6], ^{37,38}Mg [5,7], ^{40,41}Al [7], and ^{43}Si [6], as the most neutron-rich nuclei so far identified for the $Z = 9$–14 elements. For a new isotope search, accurately predicting the production cross section of neutron-rich nuclei near the drip line is very important for discussing their particle stability. However, the predictive power of the EPAX parametrization and AA models is not strong enough for specific very neutron rich nuclei [8]. For instance, although tantalum is often experimentally used as a production target to earn the better yield of these nuclei, the target dependence of production cross sections is not taken into account in these models. Instead, we first determine the production cross sections for the observed isotopes, which are then used to estimate the production cross sections and the expected yields for the nonobserved isotopes. Therefore, to enhance predictive powers for production cross sections, it is necessary to understand reaction mechanisms fully and to learn the systematic behavior of production cross sections.

The validity of the EPAX parametrization and AA models has been mainly verified for medium- and heavy-mass fragments via multi-GeV high-energy fragmentation reactions. The EPAX formula has also been used for the intermediate-energy experiments (several tens A MeV) since the formula can reproduce reasonably well even at intermediate energies the production cross sections of stable and unstable nuclei near the β-stability line. The target dependence of fragment-production cross sections in relativistic heavy-ion collisions in the EPAX formula is limited by the nuclear-size effect [9]. However, recent experiments show that the production yields of nuclei far from the stability line are quite different from the prediction of the EPAX formula, strongly depending on the N/Z ratio of the target [10]. It is of great interest to determine whether the cross sections measured with different targets factorize in projectile fragmentation at intermediate energies.

Testing the validity of factorization requires a careful measurement of the fragment momentum distribution for precise determination of the production cross sections. At

*Present address: Physics Division, Argonne National Laboratory, USA.
†Present address: RIKEN, Japan.
‡Present address: IPN, F-91406 Orsay Cedex, France.
§Present address: University of Surrey, United Kingdom.
‖Present address: Department of Physics, Kyushu University, Japan.
¶Present address: High Energy Accelerator Research Organization (KEK), Japan.
**Present address: University of Tsukuba, Japan.
††Present address: Saitama University, Japan.
‡‡Present address: TRIUMF, Canada.

relativistic energies, the shape of the momentum distribution for an isotope was found to be a Gaussian function [11] and the width was well understood with a statistical model [12]. In contrast, the momentum distribution of fragments produced at intermediate energies has an asymmetric shape with a tail at the low-momentum side. A theoretical attempt was made to reproduce the asymmetric shape, by taking into account nucleon flows between projectile and target during the collision time [13]. In this model, stochastic nucleon transfers using a Monte Carlo method and sequential evaporation were taken into account. This model can reproduce the low-momentum tails; however, because of the large friction force, the predicted distributions are shifted toward the low-momentum side much more than is observed. This discrepancy of momentum distributions leads to a large ambiguity in evaluating the production cross section from the measured yield of fragments. In addition, the measurement for very neutron rich nuclei has been performed by using very thick targets to obtain the yields, so far. Because of distortions of momentum distributions owing to target thickness, the momentum distributions of fragments cannot be clearly determined from these data. Therefore, the measurement of the momentum distribution of very neutron rich nuclei has become important.

In the present work, we focus on the target dependence of the momentum distribution of the projectile-like fragment (PLF) produced by nuclear fragmentation reactions at an intermediate energy. To investigate the target dependence of the production cross sections systematically, we used two production targets of Be and Ta. To avoid distortions of momentum distributions owing to the target thickness, we prepared relatively thin targets. We performed the experiment with the RIKEN-RIPS to eliminate the primary beam and to collect the projectile-like fragments. The data from this experiment were taken over a wide range of fragment masses including the very neutron rich side ($N/Z_f \approx 3$) toward the neutron drip line and light mass ($A_f \geqslant 3$), with good statistics for the momentum-distribution tails.

Section II describes the experimental setup and procedures. In Sec. III, the analysis of the data is explained. In Sec. IV, the observed momentum distributions of fragments, the momentum peak shift, the high- and low-momentum side widths, and the production cross sections are presented with emphasis on target dependence. On the basis of these results, we discuss the origin of target dependence in projectile fragmentation reactions.

II. EXPERIMENTAL SETUP AND PROCEDURE

The projectile fragmentation experiment using a ^{40}Ar beam was performed at the RIKEN Accelerator Research Facility. Measurements of momentum distributions of projectile-like fragments were carried out with the projectile fragment separator, RIPS [14]. The $^{40}Ar^{17+}$ beam accelerated by the ring cyclotron with energies up to 90A MeV and 94A MeV irradiated a 95 mg/cm^2 thick ^{9}Be target and a 17 mg/cm^2 thick ^{nat}Ta target, respectively.

The primary-beam intensity was monitored for normalization of fragment yields to obtain the momentum distribution. A plastic telescope consisting of three plastic scintillators with dimensions of $50 \times 50 \times 0.5$ mm^3 was placed at a backward angle of 135° degrees and at a distance of 0.5 m from the target position. The plastic detectors counted yield rates of light particles produced with nuclear reactions at the production target. The three photomultiplier tubes (PMTs) were mounted on the plastic scintillators one by one. The counting rate of triple coincidence was used to monitor the primary beam. The primary-beam intensity was measured with the indirect method of plastic counters calibrated by a Faraday cup. Calibration data were taken by changing the primary-beam intensity, which ranged from 10^{-4} to 1.0 of the full beam intensity. The systematic error of the beam monitor was estimated to be 7%.

RIPS was used as a doubly achromatic spectrometer. Projectile fragments produced at the production target and emitted at 0° were collected and transported to a double achromatic focal plane (F2). The momentum acceptance was set to be $\Delta p/p = 1\%$ at a momentum dispersive focal plane (F1), where left and right slits formed the rectangle window of momentum acceptance. The angular acceptance was set with a square window formed by four slits (upper, lower, left, and right), which were placed behind the production target. The θ and ϕ angular acceptances were 25 mrad, which is narrower than the r.m.s width of angular distribution of fragments. We use the constant value of 0.625 msr for the solid angle of $\Delta\Omega$.

Momentum distributions of fragments were measured at 23 settings of magnetic rigidity ($B\rho$) over a range of 2.520–4.068 Tm using a ^{9}Be target. With a ^{181}Ta target, the measurement of the momentum distribution for each fragment was performed at 31 magnet settings. When the magnetic field was changed for each run, the F2 image of the secondary beam was measured by means of a parallel-plate avalanche counter (PPAC) [15] to confirm transmission, and the X position of the beam at F2 was corrected to center precisely by tuning the D2 field. The beam position was monitored with an accuracy of 1 mm. The systematic error of magnetic rigidity was about 3×10^{-4} from the ratio of 1 mm to 3.6 m. The difference between D1 and D2 magnetic fields was less than 0.05%.

The identification of fragments was carried out event by event by means of measurement of time of flight (TOF) and energy deposit (ΔE) for each fixed $B\rho$ run with the 1% momentum slit. According to an estimation of the charge state distribution [16], all fragments in flight are fully striped ($Q \cong Z$). Under this assumption, the particle identification can be performed on the basis of the relations

$$B\rho \propto \frac{A}{Z}\beta, \tag{1}$$

$$\Delta E \propto \left(\frac{Z}{\beta}\right)^2, \tag{2}$$

$$\beta \propto \frac{1}{\mathrm{TOF}}, \tag{3}$$

where A and Z are mass number and atomic number, respectively.

The detectors of two 0.5-mm-thick surface-barrier-type silicon counters (SSD1, SSD2) and a 0.5-mm-thick plastic scintillation counter (PL) were installed for the ΔE and TOF

measurement at F2. Using two silicon detectors allowed us to deduce the Z number of the fragment independently, and to make correlations between them to achieve a good S/N ratio.

Both SSD1 and SSD2 have a sensitive area of 48 × 48 mm, which is wide enough to accept all particles reaching F2 where FWHM of the beam profile is 6 mm. A PMT was mounted on each side of PL (left and right). A timing of PL was determined by an averaging the signals from the left and right.

The TOF of each fragment over a 21.3-m flight path between the production target and F2 was determined from the difference of timing signals between the RF signal of the cyclotron and the PL timing. The TOF resolution was measured with a faint beam to be 0.27 ns (r.m.s.), which included the timing jitter of the RF signal (∼0.09 ns). Thus, the intrinsic resolution for the PMTs was estimated to be 0.18 ns.

III. DATA ANALYSIS

In this section we describe the procedures of the data analysis, fitting of momentum distributions, and evaluation of the production cross sections.

A. Particle identification

Figure 1 shows a two-dimensional plot of TOF versus ΔE in SSD1 for one $B\rho$ setting using the Be target. A rejection of the background events was carried out by using a correlation gate between SSD1 and SSD2. By use of the 3σ gate by two SSDs, we achieved particle identification of fragments with low background events. Fragment yields were obtained by counting the isotopes from the particle identification. Figure 2 shows the Z and A/Z projection of the particle identification at the $B\rho = 2.523$ Tm setting using the Be target. The counting gate of isotopes was a rectangle region with $\pm 3\sigma$ of the resolution σ (r.m.s.) for Z and A/Z.

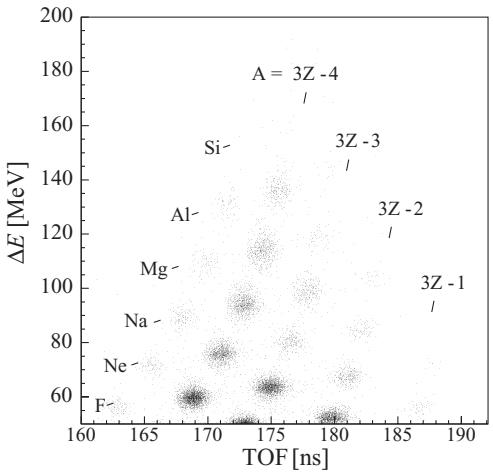

FIG. 1. Particle identification in the ΔE–TOF plane at $B\rho = 3.708$ Tm with the Be target.

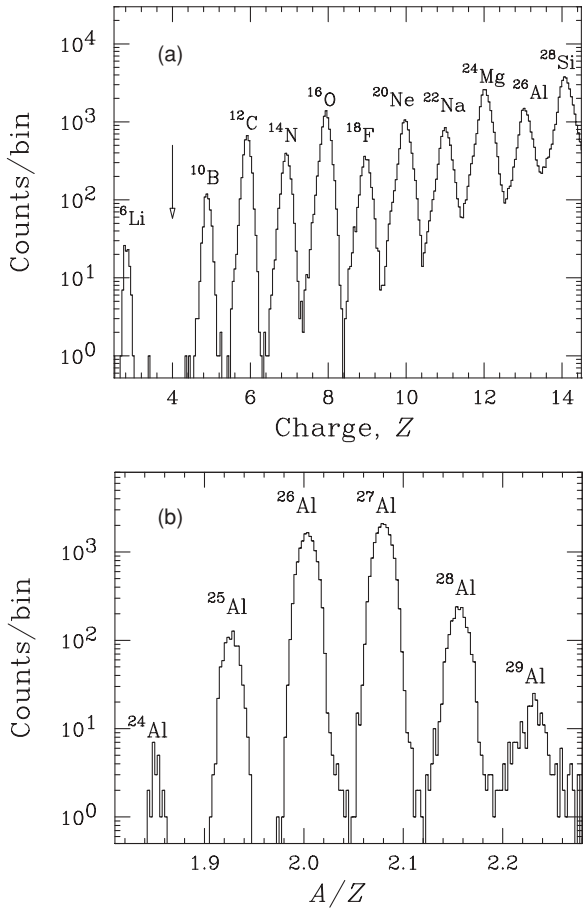

FIG. 2. (a) Z-projection spectrum for $A/Z = 2 \pm 0.3$ and (b) A/Z-projection spectrum for $Z = 13.0 \pm 0.5$ at $B\rho = 2.523$ Tm (Be target). The arrow in (a) indicates the lack of ^{8}Be, which is known to be unbound.

In the data acquired using the Be target, the analyzed isotopes were $^{6-9}$Li, $^{7-12}$Be, $^{10-15}$B, $^{11-18}$C, $^{13-21}$N, $^{15-24}$O, $^{17-27}$F, $^{19-29}$Ne, $^{21-32}$Na, $^{23-34}$Mg, $^{25-36}$Al, $^{27-38}$Si, $^{29-39}$P, $^{33-38}$S, $^{36-39}$Cl, and ^{39}Ar. Most of these isotopes are neutron-rich ones. It should be noted that the ^{36}Al, ^{37,38}Si, and ^{38,39}P isotopes analyzed have neutron numbers larger than the projectile ($N \geqslant 23$), which are produced through the neutron pick-up process. With the Ta target, we analyzed data for $^{6-8}$Li, $^{9-11}$Be, $^{10-14}$B, $^{11-17}$C, $^{13-19}$N, $^{15-21}$O, $^{17-24}$F, $^{19-27}$Ne, $^{21-29}$Na, $^{23-31}$Mg, $^{24-34}$Al, $^{26-34}$Si, $^{29-36}$P, $^{30-37}$S, $^{33-37}$Cl, $^{35-39}$Ar, and $^{37-40}$K. The potassium isotopes should be produced by the reaction with the proton pick-up process.

To obtain the doubly differential cross section from each fragment yield, we estimated the transmission between F0 to F2 and the reaction loss in the detectors. A Monte Carlo simulation by MOCADI [2] was performed under the realistic condition of RIPS using a reference beam of ^{40}Ar. The transmission value obtained was 95.3 ± 0.3%. The nuclear reaction loss of fragments in the detectors was evaluated with reaction cross sections calculated by a simple geometrical model. The reaction loss in the detectors was estimated to be less than 0.8%. The systematic error was ±9% for evaluation of the fragment cross sections.

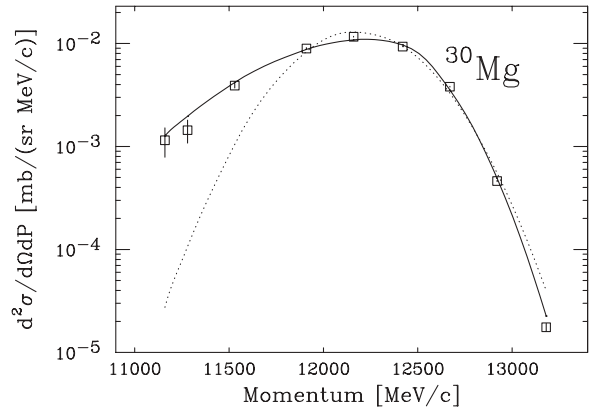

FIG. 3. Typical fragment momentum distribution and fitting results for the momentum distribution of ^{30}Mg data. The fitting result with a Gaussian function (dotted curve) shows the clearly asymmetric feature of the experimental data. The solid curve indicates a fitting result with the asymmetric Gaussian function.

B. Fitting procedure

Momentum distributions of fragments have information useful for understanding the reaction mechanisms. At relativistic energies, the projectile fragments have symmetric momentum distributions fitted to a Gaussian form. The width has been discussed with respect to the Fermi motion of nucleons or temperatures of pre-fragments [12].

The results obtained in the present work are different from those at relativistic energies. Figure 3 shows a typical momentum distribution of this experiment. Comparing the momentum distribution fitted with a Gaussian function (dotted curve), one clearly observes an asymmetric feature of the distribution. The momentum distributions of projectile-like fragments produced at intermediate energies are generally asymmetric with a tail on the low-momentum side [17].

To deduce the most probable momentum and width from such skewed shapes, the momentum distributions have been fitted with several kinds of trial functions [17–19]. Since physical models have not been established for the low-momentum tail, it is unclear what kind of functions are appropriate to use. To study systematics of the low-momentum tail, the following asymmetric function with four free parameters is applied for the present data fitting:

$$\frac{d^2\sigma}{dPd\Omega}(\theta = 0^\circ) = \begin{cases} A\exp\left[-\dfrac{(P-P_0)^2}{2\sigma_L^2}\right] & \text{for} \quad P \leqslant P_0, \\ A\exp\left[-\dfrac{(P-P_0)^2}{2\sigma_H^2}\right] & \text{for} \quad P \geqslant P_0, \end{cases} \tag{4}$$

where P_0 is the most probable peak value of momentum in the distribution and σ_L and σ_H are the momentum width in the low- and high-energy sides, respectively.

In this fitting procedure, the maximum likelihood method was used to treat the small statistics at the tails of the distributions. The result of fitting with the asymmetric Gaussian function is shown by the solid curve in Fig. 3.

By means of this method, we obtained fitting results of the momentum distribution for all the isotopes present in our data,

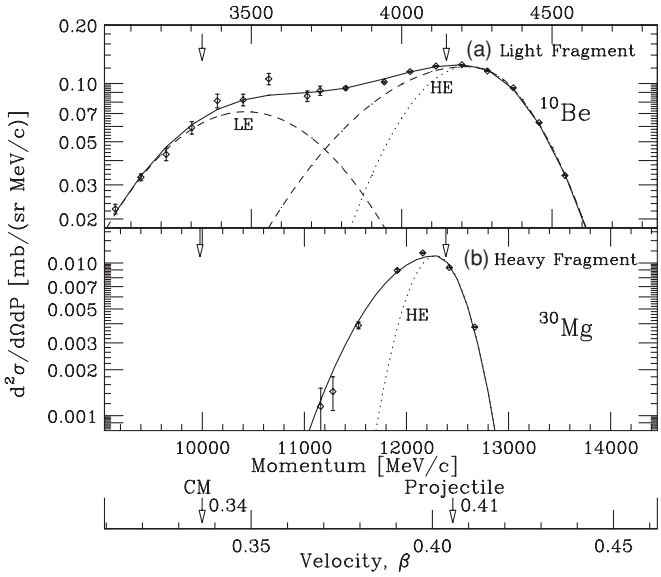

FIG. 4. Typical fragment momentum distributions for (a) ^{10}Be and (b) ^{30}Mg produced in the Ar + Be reaction. The fitting results are also shown with solid curves. The light fragment of ^{10}Be has two components (dashes curves), HE and LE; the heavy fragment of ^{30}Mg has one component, corresponding to the HE component. The HE component for each isotope has a low-momentum tail and the symmetric parts are shown with dotted curves.

though there is another kind of complexity in a few cases. We found two components in the momentum distributions of very light fragments only for the Be-target data. Figure 4 shows the momentum distributions of the ^{10}Be and ^{30}Mg isotopes from the Be-target data. Both distributions are scaled as a function of velocity (β). The two arrows in the figure indicate the velocities of projectile (β_{proj}) and center-of-mass system ($\beta_{\text{c.m.}}$), respectively. In the distribution of ^{30}Mg [Fig. 4(b)], a single component is observed near the projectile velocity (β_{proj}). However, the ^{10}Be distribution [Fig. 4(a)] shows two components at β_{proj} and $\beta_{\text{c.m.}}$. Here, the component around β_{proj} is defined as a high-energy side of the peak (HE) and that around $\beta_{\text{c.m.}}$ as a low-energy side of the peak (LE). We made an attempt to fit the data using the asymmetric Gaussian function for the HE component and a Gaussian function for the LE component. The fitting results are drawn with solid curves. The LE component decreases very quickly with increasing fragment mass number. No significant LE component has been observed for heavy fragments such as the ^{30}Mg data. Our data show clearly the LE component for the fragments with A of 9–12. The LE component has been observed for light fragments in the Ar + Be reaction, whereas the LE component has not been found in the momentum distributions of Ar + Ta reaction data in the momentum region where the experimental data were taken. When a light fragment such as ^{10}B is produced in the Ar + Ta reaction, the impact parameter is much larger than in the case of the Ar + Be reaction. Thus, we found the LE component only for the Ar + Be system. Since we focus on the projectile fragmentation reaction, we discuss mainly the HE component in this paper.

C. Evaluation of cross sections

The production cross sections of fragments were evaluated with the fitting results of the longitudinal momentum distributions. The transverse momentum distributions are assumed to be a Gaussian function with a width of $\sigma_\perp$,

$$\sigma_\perp^2 = \sigma_H^2 + \frac{A_f(A_f-1)}{A_p(A_p-1)}\sigma_D^2, \tag{5}$$

where σ_D is a parameter of the deflection effect and A_p and A_f are mass numbers of projectile and fragment, respectively. Van Bibber *et al*. [20] have shown the deflection parameters for the two targets of ^{27}Al and ^{197}Au with ^{16}O beams at 92.5 and 117.5A MeV. The results from their measurement were $\sigma_D = 190$–220 MeV/c, without strong target dependence. Taking account of an energy dependence reported in Ref. [21], we used σ_D of 195 MeV/c around 90A MeV for the present experiment. The ambiguity of transverse momentum distributions was taken into account as the systematic error of the cross sections. The overall systematic error for the production cross sections is shown in Fig. 5.

IV. RESULTS AND DISCUSSION

The fitting results with the asymmetric Gaussian function are presented in the following. First, the fitting results of the momentum distributions are compared with several formulas taken from reaction models. The result for the high-momentum side width can be understood by the Goldhaber model. However, we need further discussion of the momentum peak shift and low-momentum side width. Next, we show the result of production cross sections, which reveals the phenomena of breakdown of factorization (BOF) for the production of very neutron rich nuclei. We discuss the systematics of isotope production cross sections. The charge distribution of the cross sections for a fragment mass is obtained from our data and compared with the EPAX formula. Finally, we discuss the pre-fragment production mechanism in projectile fragmentation reactions to search for the origin of the BOF.

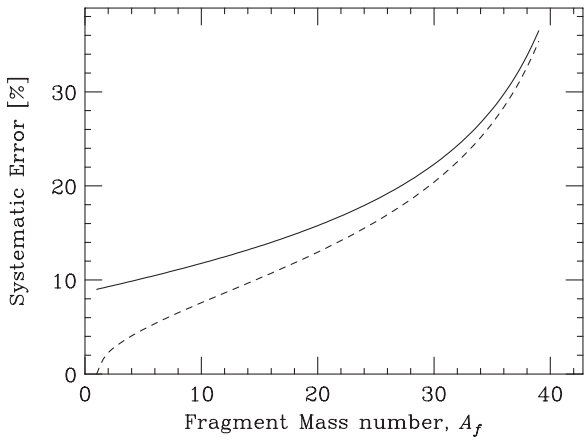

FIG. 5. Overall systematic error for the production cross sections (solid line). The dashed line shows error originating from the ambiguity of $\sigma_\perp$.

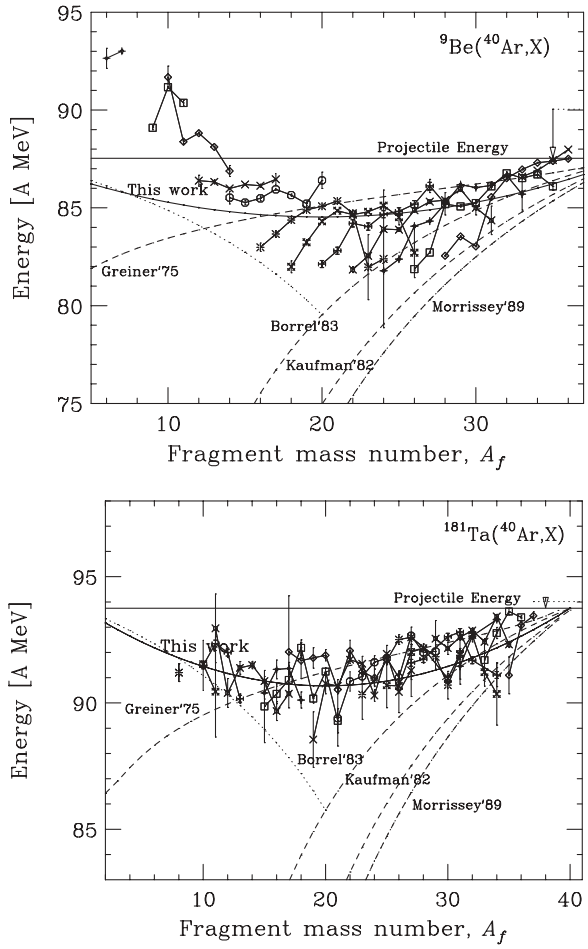

FIG. 6. Momentum peak shift of fragments produced in Ar + Be (upper panel) and Ar + Ta (lower panel). The primary beam energies are drawn with dotted lines, and the kinetic energies at the half-point of target thickness (projectile energies) are the solid lines. See the text for the labels and curves.

A. Momentum peak shift

In the nuclear fragmentation process, part of the projectile kinetic energy is converted into excitation energies of fragments, and the projectile velocity is decreased. This energy loss in projectile fragmentation is called the "momentum peak shift." The momentum peak shift is obtained from the difference of the projectile velocity and the most probable velocities of the fragments. We present the result of momentum peak shift in units of energy per nucleon, which is proportional to the square of velocity. These units are convenient for discussing kinetic energy consumption in nuclear reactions.

Figure 6 shows the momentum peak shift of fragments produced in Ar + Be and Ar + Ta reactions. The solid lines for each isotope are drawn to guide the eye. The primary-beam energies were corrected with the mean energy loss in the production target. The obtained projectile energies (solid lines) were taken to be 87.5A MeV and 93.8A MeV, respectively. The values of the most probable energies of fragments were also corrected with energy losses in the targets. The negative shift

of the data from the solid line of the projectile energy indicates the energy loss by the nuclear fragmentation process.

The systematic error of momentum shift was estimated to be 0.9% in units of energy per nucleon.

The deviation for a given element chain in the Be target is comparable to the systematic error. As seen in Fig. 6, the measured momentum shifts for the Be target (a), compared with the case of the Ta target (b), vary widely. One could understand the deviation as an effect of the target thickness in the atomic energy-loss process [22], because the target thickness of Be is six times that of Ta.

In the results for both targets, we found that the momentum peak shift has a parabolic mass dependence over a wide range of fragment masses. The momentum peak shift increases when the number of removed nucleons $\Delta A = A_p - A_f$ is increased up to half of the projectile mass ($A_f \geqslant 20$). However, the momentum shift decreases when the mass loss ΔA is increased beyond 20 ($A_f < 20$). In short, we observed the maximum momentum peak shift around $A_f = 20$.

The phenomenon of fragment acceleration was observed in the Be-target data. In Fig. 6(a), the solid line of 87.5A MeV corresponds to the primary-beam energy. Velocities of the fragments ^{6,7}Li, $^{9-11}$Be, and $^{10-13}$B are larger than the projectile velocity. The very light fragments are accelerated in the reaction process. We note that the acceleration phenomena was also observed in collisions of ^{238}U at 1A GeV with lead, reported by Enqvist *et al.* [23]. However, no acceleration for any fragments with $A_f \geqslant 8$ was observed in the Ta-target data. Except for the acceleration phenomenon, no significant difference between the targets was observed in the momentum peak shift for the projectile-like fragments with $A_f \geqslant 20$.

We found two features in the momentum peak shift. First, the maximum of the momentum peak shift is observed for the fragments around $A_f = 20$ in Fig. 6 for both targets. Second, the acceleration phenomenon was observed in light fragments only for the Be target. Namely, the most probable velocities of light fragments are beyond the projectile velocity. In the following, we discuss the features observed in the momentum peak shift.

1. Parabolic mass dependence of peak shift

The momentum peak shift has been investigated for a long time. Many of the reports have shown a linear mass dependence of the peak shift for fragments with $A_f \geqslant A_p/2$. Several formulas proposed so far reproduce the momentum peak shift for the heavy fragments produced in peripheral collisions. We compare our experimental results for the wide fragment mass range with the formulas and make an attempt to introduce a new picture to reproduce the parabolic mass dependence.

In Fig. 6, four formulas are shown with dashed curves and labeled as Greiner75, Kaufman82, Borrel85, and Morrissey89 [24–30]. For every formula, the momentum shift becomes large when the number of removed nucleons, ΔA, is increased. This tendency conflicts with the present result in the region of $A_f \leqslant 20$. To compensate for the deviation, Winger *et al.* [1] obtained a formula symmetrized mathematically with respect to $A_p/2$ (dotted line). However, it still overestimates the momentum shift around $A_f \sim A_p/2$. None of these formulas can predict the parabolic mass dependence.

The previous studies were mainly performed in the region of fragments close to the projectile mass. For the whole fragment mass region observed in this work, a parabolic dependence, where the symmetric point is at the half mass of the projectile, is observed. As Borrel first commented [30], the symmetric behavior of the velocity shift implies another mechanism, which is less costly than the removal of individual nucleons. The mechanism may be a process that the projectile splits into two pieces. We deduce a semiempirical formula by considering the excitation energy of fragments. The splitting process consumes the kinetic energy of the projectile.

Here we assume that the energy consumption is proportional to the number of pairs of nucleons destroyed in the reaction, where the nucleons act mutually by a long-range force. In this picture, the number of pairs of nucleons in the projectile is counted with ${}_{A_p}C_2 = A_p(A_p - 1)/2$, where the mark of ${}_nC_m$ is the combinatorial that gives the number of ways of choosing m out of n. When the projectile splits into the spectator A_f and the participant $(A_p - A_f)$, the number of pairs of nucleons decreased in the reaction serves as $A_f(A_p - A_f)$. When one nucleon is removed ($A_f = A_p - 1$), the decreased number of pairs is $A_p - 1$, and the total energy loss can be defined as ε MeV. The energy loss per nucleon pair is $\varepsilon/(A_p - 1)$ MeV on average. Thus, the kinetic-energy loss in the splitting process can be written as

$$\Delta E = \frac{\varepsilon A_f(A_p - A_f)}{A_p - 1}. \tag{6}$$

In the case of nonrelativistic beam energy, energy conservation between the projectile and the two pieces gives a new parametrization as follows:

$$\frac{v_f}{v_p} = \sqrt{1 - \frac{\varepsilon A_f(A_p - A_f)}{A_p E_p(A_p - 1)}}. \tag{7}$$

If we select the energy loss parameter of $\varepsilon = 8$ MeV, this formula corresponds to Borrel's model for the case of one-nucleon removal. However, the value of ε may not be 8 MeV. In Fig. 6, the P_0 values predicted by the formula were compared with the present data. The solid curve (this work) was drawn with $\varepsilon = 12$ MeV to fit the data. The experimental data support that $\varepsilon = 12$ MeV is better than 8 MeV.

2. Acceleration phenomenon

The acceleration effect cannot be explained by a fragmentation model based on the abrasion-ablation picture, in which the projectile always loses the kinetic energy in the laboratory system for the abrasion process of nucleons.

The acceleration phenomenon may be peculiar to the ^{9}Be(^{40}Ar, X) reaction, namely, inverse kinematics. No acceleration effect was found in the Ta-target data. By comparison of the targets, we found two particular features of momentum distributions for light fragments produced in the Ar + Be reaction. One feature is the acceleration phenomenon. The

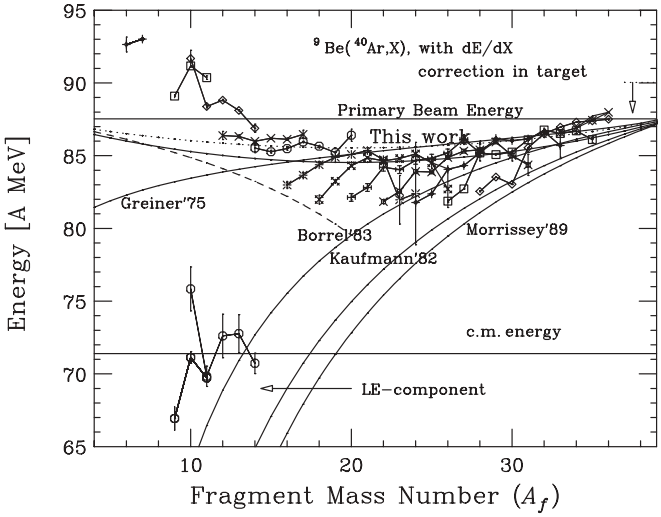

FIG. 7. Peak value, P_0, of fragment momentum distribution for HE and LE components.

other feature is the existence of the LE component. Both phenomena coincide in our data. Therefore, the acceleration phenomenon may be related to the LE component.

The LE component of the lightest fragments, which was only observed with the Be target, would be related to multifragmentation. As shown in Fig. 7, the velocities of the LE component observed in this work are just from the c.m. velocity of the incident system. It is natural to speculate that the source of the LE component is a highly excited compound system generated via central collision.

The origin of the acceleration phenomena could be understood by microscopic model calculations. Shi *et al.* [31] studied the interplay between spectator and participant matter in the context of a microscopic transport model. According to the simulations of the projectile fragmentation reaction, the post-acceleration of the light fragments is interpreted as the response of the projectile spectator to the participant blast. The spectators pass by the participant region when the participant matter undergoes a violent explosion. The explosion pushes the spectators, giving them transverse momentum, which is pointed away from the reaction zone. If the explosion is strong enough to overcome the friction effects, the net spectator momentum per nucleon increases along with post-acceleration. Benlliure *et al.* [32] performed an experiment using a high-resolving-power magnetic spectromenter to isotopically identify the projectile-like fragments produced in relativistic heavy-ion collisions and determine their velocities with high precision. They observed the dependence of the post-acceleration of the projectile-like fragments with the size of colliding nuclei and beam energies.

From the result of our experiment, we can speculate that the origin is related to the impact parameter. Neither the acceleration effect nor the LE component was found in the Ta-target data. The different situation for the Be target comes from the large impact parameter. For a certain fragment mass, the impact parameter in the Ar + Ta reaction is larger than that in the Ar + Be reaction when the fragment is formed by the geometrical cut. The hot compound system is not produced

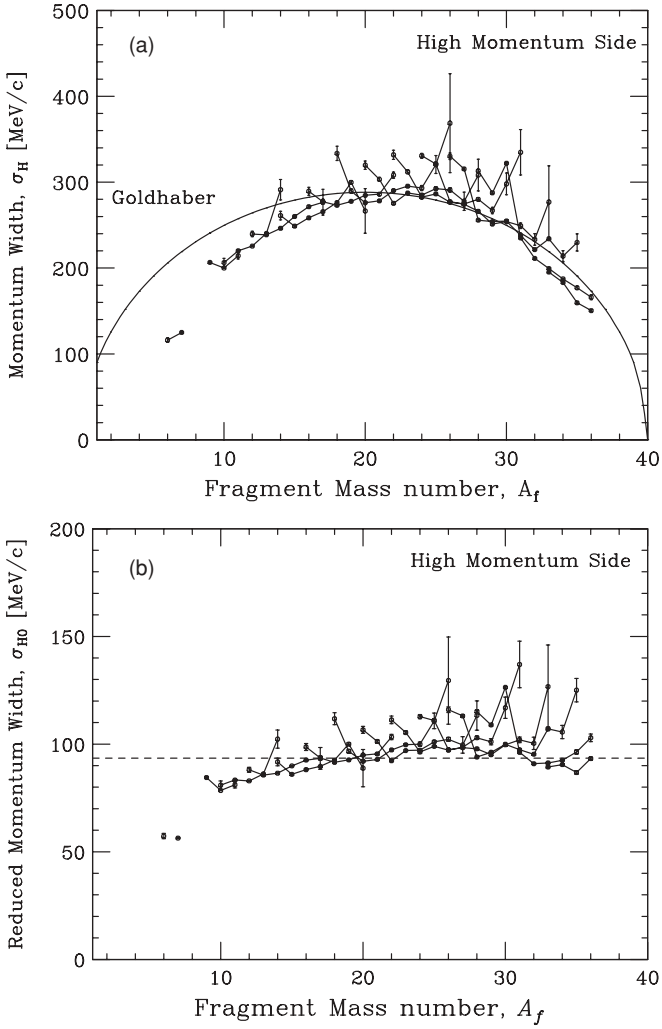

FIG. 8. Momentum widths at high-momentum side (Be target) for (a) σ_H and (b) reduced widths according to the Goldhaber model.

in the peripheral collision with the large impact parameter. Therefore, the exotic phenomena may not be observed in the Ta-target data.

B. High-momentum side width

The high-momentum side widths σ_H as a function of fragment mass are shown in Fig. 8(a) and Fig. 9(a), for the Be and Ta targets, respectively. The high-momentum side widths of all the observed fragments are compared to the formulation by Goldhaber as follows:

$$\sigma_{||} = \sigma_0 \sqrt{\frac{A_f(A_p - A_f)}{A_p - 1}}, \tag{8}$$

where A_p and A_f are the mass number of the projectile and fragment, respectively. The solid curves are drawn with the reduced width $\sigma_0 = 90$ MeV/c from experimental results at relativistic energies [12]. The deduced values of σ_0 for the fragments in the mass range 9 to 36 are shown in Fig. 8(b) and Fig. 9(b). The dashed lines denote the mean value of $\sigma_0 = 93.5 \pm 2.6_{\text{stat}} \pm 7.5_{\text{sys}}$ for the Be target, and

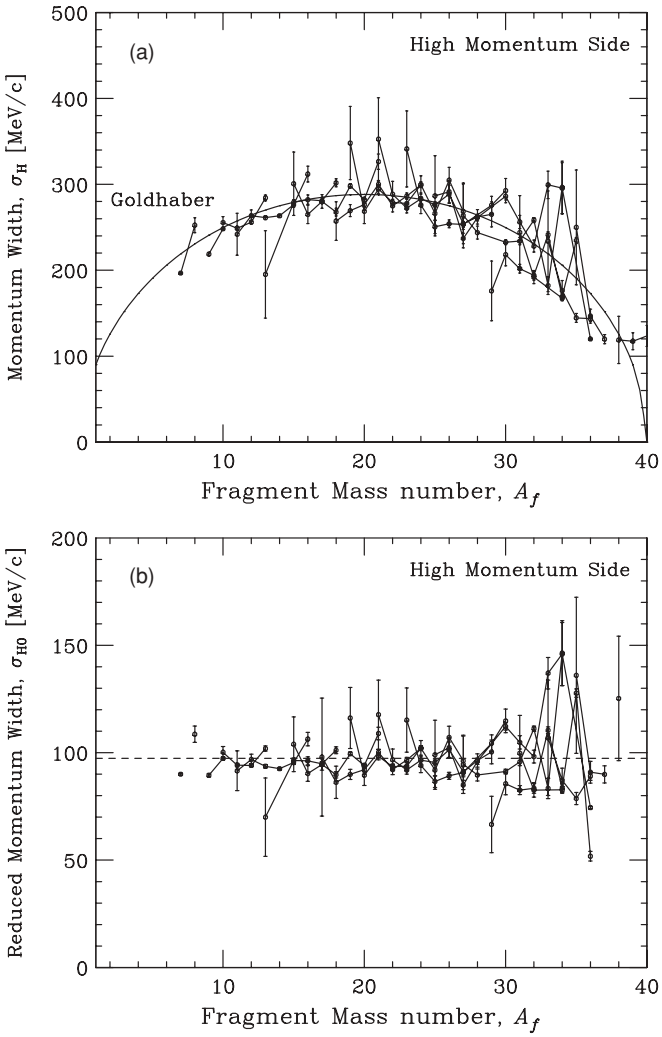

FIG. 9. Momentum widths at high-momentum side (Ta target) for (a) σ_H and (b) reduced widths according to the Goldhaber model.

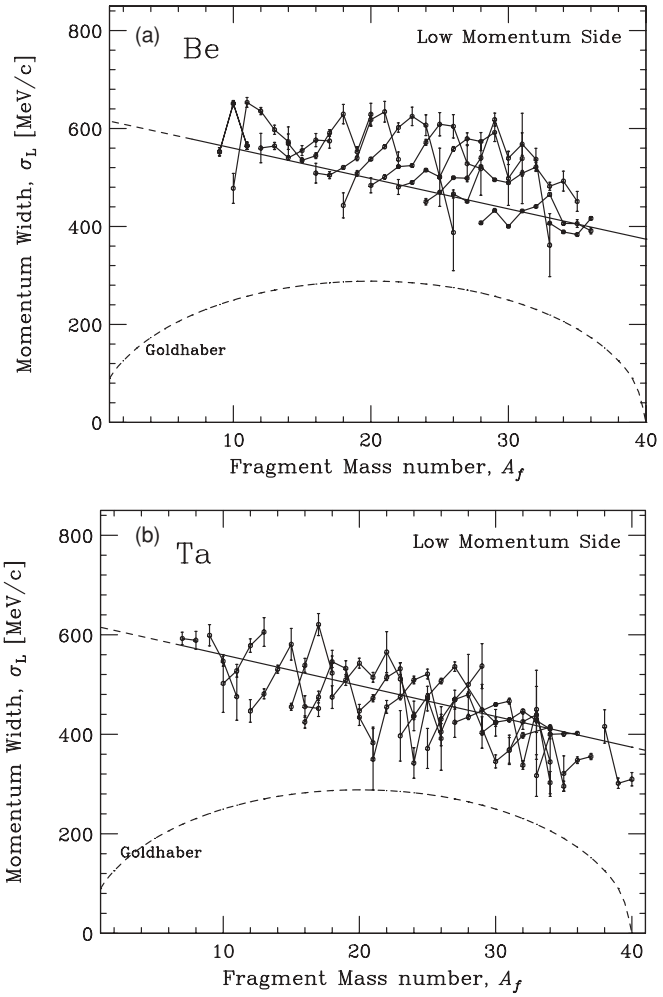

FIG. 10. Momentum widths at low-momentum side by using (a) the Be target and (b) the Ta target. The solid lines in both figures are the linear fits of the Ta target data. The experimental results (σ_L) and the fitting lines are located far from a prediction of the Goldhaber model. The isotope chains of experimental data are also drawn as solid lines.

$97.4 \pm 1.8_{\text{stat}} \pm 7.8_{\text{sys}}$ MeV/c for the Ta target, respectively. No significant difference between the targets was observed in the high-momentum side widths. The light fragments $A_f < 13$ produced by using the Be target show a slight deviation from the Goldhaber model. The deviation originates from the LE component and the fitting function to be used. To avoid a digression from the main purpose, we do not discuss this deviation further. These results are in good agreement with high-energy experiments [12].

At relativistic energies, the reduced width σ_0 is independent of the primary beam energy. At lower energies, the reduction of σ_0 has been observed [33]. The reduction mechanism has been discussed in several theoretical works, where, for example, Pauli blocking is suggested. Because of this effect, σ_0 has an energy dependence at 30–40A MeV [29,34] and becomes constant up to 90A MeV. The fact that the measured σ_0 is the same as the high-energy one is consistent with this picture.

C. Low-momentum side width

The results of momentum width at the low-momentum side are shown in Fig. 10. The widths of the low-momentum side, σ_L, are plotted as a function of fragment mass with their statistical errors. We compared the results with the high-momentum side width σ_H. Instead of showing individual data of σ_H, the dashed curve calculated with the Goldhaber model is presented. The systematic error of σ_L is estimated to be 8%, which is not shown in the figure.

In the Be-target data, each isotope chain has a mountain-style structure (solid curves). However, the low-momentum widths σ_L of the Ta data may have no such structure. One can understand the deviation as a target thickness effect. Another reason for the mountain-style structure should be noted. The momentum distribution of light fragments has the LE component at the low-momentum side only for the ^{9}Be target data. In the fitting procedure with an asymmetric Gaussian-like function, the LE component may also affect the results. Therefore, the mountain-style structure of σ_L for fragment mass should be ignored and treated as a systematic error.

As seen in Fig. 10, the measured widths of σ_L are approximately twice those of σ_H. Obviously, the large width cannot be explained by the Goldhaber model. The σ_L may have a linear dependence as a function of mass loss, $\Delta A = A_p - A_f$, which is very different from the parabolic feature of σ_H. No significant target dependence of σ_L between the Be and Ta targets was found in our data. As no models for the low-momentum tail have been established, it is difficult to discuss the low-momentum tail only from the systematics of σ_L. Yet we should comment that the low-momentum tail may not depend on the target.

In addition, at the limit $\Delta A \to 0$, the σ_L may not converge to 0, but to 300–400 MeV/c. This feature differs from the Goldhaber formula. Even if the fragmentation reaction is the dominant process for production of fragments, these new observations may lead to an additional reaction process necessary for intermediate-energy reactions.

In Fig. 10, a fitting line was first obtained from the Ta data. The fitting lines are drawn in both figures. The experimental results (σ_L) and the fitting lines are located far from a prediction of the Goldhaber model.

What is the origin of the large width of the low-momentum side? The large width is indeed produced by an energy-loss process in the nuclear reaction. The energy-loss process for σ_L may be different from the "pure" fragmentation process, because the width of low-momentum side strongly depends on the beam energy. At relativistic energies, the momentum distribution becomes symmetric with $\sigma_L = \sigma_H$. For a low-energy beam at 30A MeV, the obvious large tail of the low-momentum side appears [35]. The macroscopic friction process of nuclear dissipation is not a satisfactory mechanism for σ_L because the momentum peak P_0, which has no significant energy dependence, may also change at the same time.

The energy-loss process to produce the width of the low-momentum side may be explained by a nucleon-exchange reaction between target and projectile [36]. For instance, if the transfer mechanism adds one nucleon to the projectile or fragment, the energy per nucleon E may be modified as $E_{+1n} = EA/(A+1)$, where A is the mass number before transfer reaction. Since the projectile velocity is reduced by the nucleon-exchange reaction, the nucleon transfer may contribute to the low-momentum tail. When the projectile gives a nucleon to the target nuclei, the velocity of the remaining nucleons in the projectile does not change significantly. Like the effect of the momentum peak shift, the change of potential energy in the projectile slightly affects the velocity of the projectile nucleus. However, when the projectile picks up one nucleon from the target nuclei, the projectile velocity should be reduced because nucleons in the target nuclei are much slower on average in the laboratory system. Thus, we suppose the nucleon-exchange reaction as an origin of the low-momentum tail.

Under the assumption that the probability of nucleon exchange is described as a Poisson distribution and that the average number of transfer nucleons in a reaction is quite small, the transfer process does not contribute to the peak shift of fragment momentum distribution but causes the large width of the low-momentum tail. If the probability of the transfer process is small on average, the peak shift of the fragment momentum distribution, which is related to the case of no nucleon transfer, does not suffer from the transfer process toand is independent of the beam energy. However, the low-momentum width is sensitive to the transfer probability.

We next discuss the linear dependence of σ_L as a function of ΔA. First, we try to explain this dependence in terms of the surface abraded. If the transfer probability is proportional to the surface area, the probability may be described as a symmetric function with respect to half the projectile mass. However, the observed behavior has a linear dependence. So, the abraded surface may not be directly related to the transfer process.

Second, we consider the overlap volume of projectile and target nuclei (i.e., the total number of nucleons in the participant region). The region has nearly a linear dependence as a function of A_f. Thus, the linear dependence of σ_L may be related to the volume of the overlapped region.

D. Transfer-like fragmentation

The transfer-like fragments of ^{36}Al, ^{37,38}Si, ^{38,39}P, and $^{37-40}$K were observed for this experiment. These fragments have more neutrons or protons than the projectile nucleus. The fragments cannot be produced with projectile fragmentation reactions. Neutron and proton pick-up processes are necessary for production of the fragments.

Figure 11 shows the momentum distribution of ^{36}Al acquired by using the Be target. This isotope production needs at least one neutron pick-up process from the target nucleus. We made an attempt to fit the momentum distribution with an asymmetric Gaussian function. Because of the lack of data at the low-momentum tail, we assumed that the fitting parameters of momentum widths were fixed. The σ_H value was taken from the Goldhaber formula with $\sigma_0 = 90$ MeV/c.

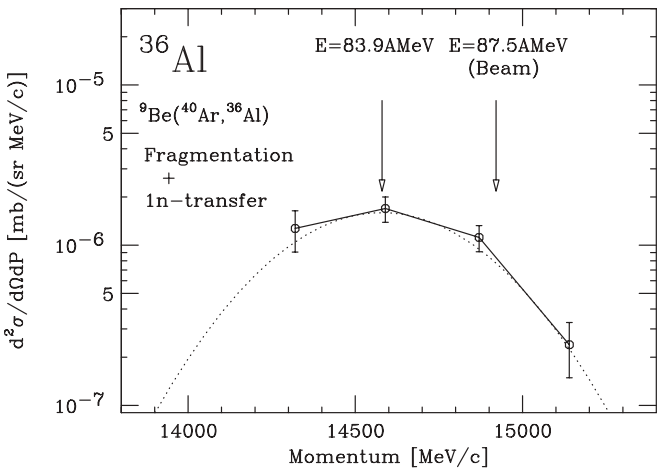

FIG. 11. Momentum distribution for ^{36}Al. This isotope cannot be produced with only the nuclear fragmentation process. One neutron should be picked up from the target. The measured peak momentum corresponds to 83.9A MeV. The measured momentum peak shows a larger shift toward the low-momentum side, compared with that of the same mass number, ~0.9A MeV.

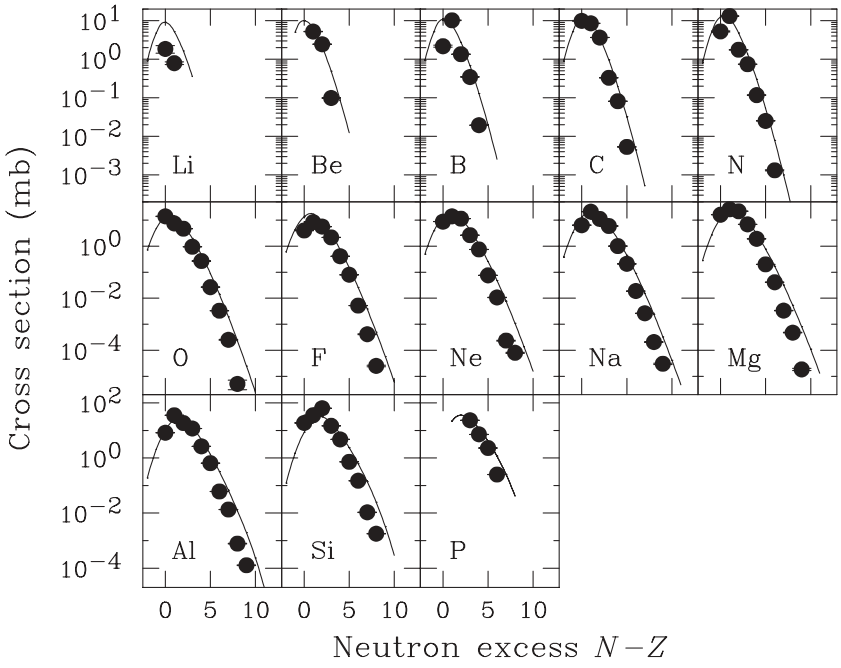

FIG. 12. Measured cross sections presented as isotope distributions for $3 \leqslant Z \leqslant 14$ elements detected in $^{40}\mathrm{Ar} + {}^{9}\mathrm{Be}$ reactions at 90 MeV/nucleon. Experimental fragmentation data are shown as filled circles. EPAX predictions are shown as solid curves.

The σ_L was assumed to be $400 \pm 60_{\mathrm{sys}}$ MeV/c. This value was obtained from the systematics as shown in Fig. 10.

The fitting result is shown as a dotted curve in Fig. 11. The peak of the momentum distribution corresponds to 83.9A MeV. The primary beam energy was measured as 87.5A MeV, and so the momentum peak shift was obtained as $3.6 \pm 1.2A$ MeV.

The measured momentum peak shows clearly a larger shift toward the low-momentum side, compared with that of the same mass number, $\sim$0.9A MeV. The large momentum shift of transfer-like fragments was also observed in the fragments of $^{37-40}$K requiring a proton pick-up process in production.

E. Target dependence of cross sections

The target dependence of cross sections was investigated with the results of our experiments. We have obtained the cross sections over a wide range of fragment charges for each fragment mass with small statistical and systematic errors, and for the same projectile (^{40}Ar) with two sets of targets (^{9}Be and ^{181}Ta). All the measured cross sections are shown in Figs. 12 and 13, so we can investigate the validity of factorization for fragmentation reactions at intermediate energies.

Figure 14 shows the ratios of cross sections for a fragment in Ar + Ta reactions to those in Ar + Be reactions. The cross sections are normalized with the experimental mass yield

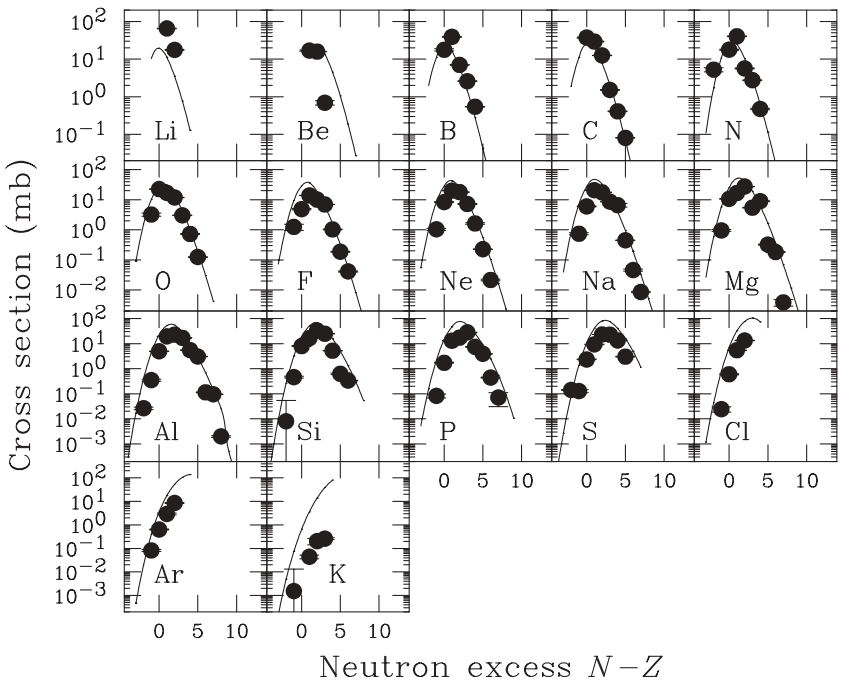

FIG. 13. Measured cross sections presented as isotope distributions for $3 \leqslant Z \leqslant 19$ elements detected in $^{40}\mathrm{Ar} + {}^{181}\mathrm{Ta}$ reactions at 94 MeV/nucleon. Experimental fragmentation data are shown as filled circles. EPAX predictions are shown as solid curves.

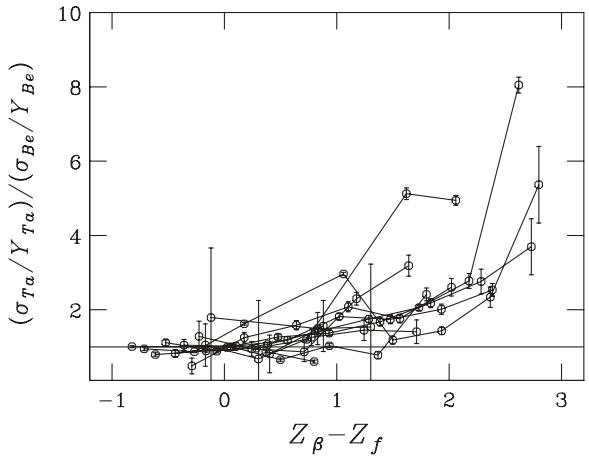

FIG. 14. Ratio of the production cross sections for each fragment produced with Be and Ta targets. The solid lines are drawn for the same mass number of nuclei (i.e., isobars). The Z_β is the β-stable charge for each isobar. The cross section ratio of $\sigma_{\mathrm{Ta}}(A, Z)/\sigma_{\mathrm{Be}}(A, Z)$ is normalized with the mass-yield ratio of $Y_{\mathrm{Ta}}(\mathrm{A})/Y_{\mathrm{Be}}(\mathrm{A})$ observed.

$Y(A_f)$ to eliminate the target-size effect. The mass yields were obtained from the sum of fragment cross sections with the same mass number. The ratio is shown as a function of charge difference between the most stable charge $Z_\beta(A_f)$ and the fragment charge Z_f. Thus, the target dependence of projectile fragmentation cross sections except for the target-size effect is represented over a wide range of isotopes near and far from the stability line. If the factorization is valid for production of an isotope, the ratio has no $Z_\beta - Z_f$ dependence.

In Fig. 14, the ratios near the β-stability line are constant, indicating that the factorization is valid for the production of the nuclei. According to previous work [37], the factorization is valid for the isotopes $Z_\beta - Z_f \leqslant 2$. However, the ratios increases when $Z_\beta - Z_f$ is increased. This deviation shows that the factorization hypothesis is clearly broken down for neutron-rich nuclei with $(Z_\beta - Z_f) \geqslant 2$.

F. EPAX formula

The EPAX formula was developed by using data of the spallation reactions and heavy-ion induced fragmentation reactions at several A GeV [38]. The cross section of a fragment with mass A and proton number Z produced by projectile fragmentation from a beam (A_p, Z_p) impinging on a target (A_t, Z_t) can be written as

$$\sigma(A, Z) = Y(A)W(A, Z), \tag{9}$$

$$W(A, Z) = n \exp(-R|Z_{\mathrm{prob}} - Z|^U), \tag{10}$$

where $Y(A)$ represents the mass yield, which is the sum of the isobaric cross sections for fragments with mass number A, and $W(A, Z)$ describes the charge distribution, which means the cross section distribution of a given fragment mass that has a maximum peak at Z_{prob}.

The charge dispersion $W(A, Z)$ is described by R, Z_{prob}, and the U parameter. The most probable charge, Z_{prob}, is written as

$$Z_{\mathrm{prob}} = Z_\beta + \Delta + \Delta_m, \tag{11}$$

where Z_β is the β-stable charge for a certain fragment of mass number A, Δ is a proton excess between the stability line and the most probable line of the fragmentation reaction, and Δ_m is the so-called memory effect (i.e., the influence of the projectile N/Z ratio on the fragment N/Z ratio). The width parameter R is a function of fragment mass number A, which shows a fragment mass dependence on steepness-controlling cross sections of isotopes from the stability line to the drip lines. The mass dependence has been confirmed by using many combinations of projectiles and targets. The U parameter is given as a constant for all neutron-rich isotopes so far.

By using new data obtained mainly at the GSI/FRS facility, the EPAX formula was recently modified [3] slightly to tune the mass yield and the U parameter for proton-rich fragments in the vicinity of projectiles. The present paper focuses on the neutron-rich fragments over a wide range of fragment A and Z. Thus, this work gives analysis and discussion of the EPAX formula based on the original EPAX, which has relatively simple functions.

The EPAX formula is valid for the "limiting fragmentation" regime, where the fragmentation process is no longer energy dependent. The energy dependence of fragmentation cross sections has been investigated by Silberberg and Tsao [39,40]. We can see a similar energy dependence in the total reaction cross section. The total reaction cross section has been studied both theoretically and experimentally for more than 50 years. A detailed list of references is found in Ref. [41]. The difference between the cross sections of $^{12}\mathrm{C} + {}^{12}\mathrm{C}$ at 90A MeV and at 900A MeV is about 30% [42]. This value is nearly equal to the systematic error of the measured cross sections in this work. Thus, we can assume that the limiting fragmentation hypothesis is valid in this work.

The EPAX formula follows the factorization hypothesis. The mass yield has a target dependence; however it is limited to the target nuclear-size effect. The charge dispersion $W(A, Z)$ is independent of the target nucleus.

In this work, however, the BOF has been found in the production of very neutron rich nuclei. An investigation of the charge distribution is necessary to find an appropriate description for cross sections from our data. In the charge distribution of EPAX, the U parameter is a constant 1.65 for the neutron-rich side and has no target dependence. The value of the U parameter is very sensitive to the production cross sections of the isotopes far from the β-stability line. In the following, we deduce the U parameter for each fragment mass with both targets from our data. At the same time, we investigate the target dependence of Z_{prob} since Z_{prob} is also sensitive to the cross sections of isotopes far from the β-stability line.

1. Charge distribution

A fitting of the production cross sections was performed by using the EPAX function. The function is represented as the product of $Y(A)$ and $W(A, Z)$. The charge distribution

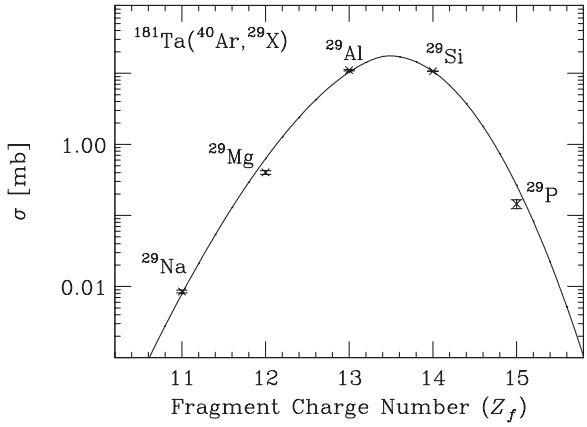

FIG. 15. Charge distribution for $A_f = 29$.

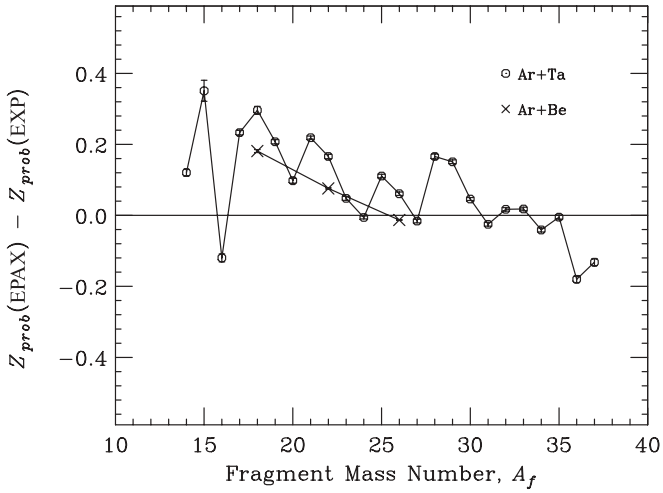

FIG. 16. Deviation of the most probable charge from the EPAX parametrization to experimental data for the production targets of Be and Ta.

$W(A, Z)$ is characterized with the most probable charge Z_{prob}, the slope constant U, and the width parameter R. The R parameter depends slightly on fragment mass and is affected by the slope of the charge distribution. We have two kinds of U parameters: U_p for the proton-rich side and U_n for the neutron-rich side. In the fitting procedure, the values of the U_p and the R parameters are fixed, originally given by the EPAX formula. The fitting procedure was performed with the experimental data of each fragment mass. First, we obtain the maxima of the charge distribution Z_{prob}(EXP) as a function of fragment mass number from the experimental data with both targets. The values are compared with the EPAX ones, the β-stability line, and the N/Z ratio of projectile nuclei. Next, the U parameters are deduced from the data when we assume the same parametrization of Z_{prob} for both targets.

We have investigated the target dependence of Z_{prob}. The measured cross sections for each fragment mass were fitted with $Y(A) \times W(A, Z)$. The mass yield Y is a constant for a certain fragment mass. Fitting parameters were the U parameter for neutron-rich side, Z_{prob}, and the mass yield. Figure 15 shows the charge distribution of fragment mass 29, produced in the Ar + Ta reaction. The Z_{prob} is obtained as $13.47 \pm 0.01_{\text{stat}} \pm 0.04_{\text{sys}}$. Similarly, the Z_{prob} value for each fragment mass is deduced from our experimental data.

The experimental Z_{prob} is compared with the value from the EPAX formula. Figure 16 shows the deviation of Z_{prob} (EXP) from Z_{prob} (EPAX) for Ar + Be and Ar + Ta data. Solid lines are drawn to guide the eye. The EPAX formula reproduces the Z_{prob} very well, especially for mass numbers between 20 and 35. The deviation of Z_{prob} is less than 0.2. Because of the lack of data on the proton-rich side, we obtained only three values of Z_{prob} for the Ar + Be data in $A_f = 18$, 22, and 26. Comparison of the data from Be and Ta targets shows no significant target dependence of Z_{prob}.

Figure 17 shows the most probable charge in N/Z units as a function of fragment mass for the Be and Ta targets. The most probable charge Z_{prob} from the EPAX is close to the β-stable charge Z_β. The ratio N_p/Z_p of the projectile is 1.22. For the composite system of projectile and target, the ratio is represented as $(N_p + N_t)/(Z_p + Z_t)$, with values of 1.23 and 1.43 for Ar + Be and Ar + Ta, respectively. The Z_{prob} (EXP) is well described as Z_{prob} (EPAX) as well as Z_β. The difference between Z_{prob} (EPAX) and Z_β is mainly the memory effect Δ_m, which is not clearly seen in our data.

No significant difference of Z_{prob} (EXP) between the Be and Ta targets has been observed; however, the BOF has been found in the very neutron rich nuclei. What does this mean? It should be noted that the BOF had never been found in projectile fragmentation in other experiments. This is consistent with our observation of Z_{prob} (EXP) for the Be and Ta targets. To understand the charge distribution, we show the Z_{prob} of projectile-like fragments produced by the reactions at low and intermediate energies.

At low energies, the most probable charge shows the existence of two different reaction mechanisms. In Ref. [43], Cl isotopes were produced in the 7A-MeV ^{40}Ar + ^{50}Ni reaction and the contour plots of the Cl isotope yield were drawn as the function of fragment mass and kinetic energy. We clearly see two components, one corresponding to quasi-elastic reactions centered at a high energy and a mass of 39, and the other centered at a low kinetic energy and a mass of 36. The most probable charge obtained from the mass number is near the N/Z of both the projectile and the composite system, corresponding to the quasi-elastic and deep inelastic reactions, respectively [44].

An intermediate composite system has been shown as the result of a complete damping of the relative motion between the projectile and target nuclei. The projectile-like fragments are produced via a binary nuclear system in which collective effects dominate. However, at high energies, the process is dominated by individual nucleonic collisions that are described as participant-spectator models. The values of the most probable charge distinguish the reaction mechanisms to produce the projectile-like fragments.

At intermediate energies, Guerreau *et al.* [45] reported the observation of the systematic shift of isotope distributions between the two targets. The isotope distributions of fragment yield were measured in the ^{40}Ar + Ni and the ^{40}Ar + Au reactions at 44A MeV. The systematic shift of the isotope distributions for a given element of Si in the ^{40}Ar + Au reaction

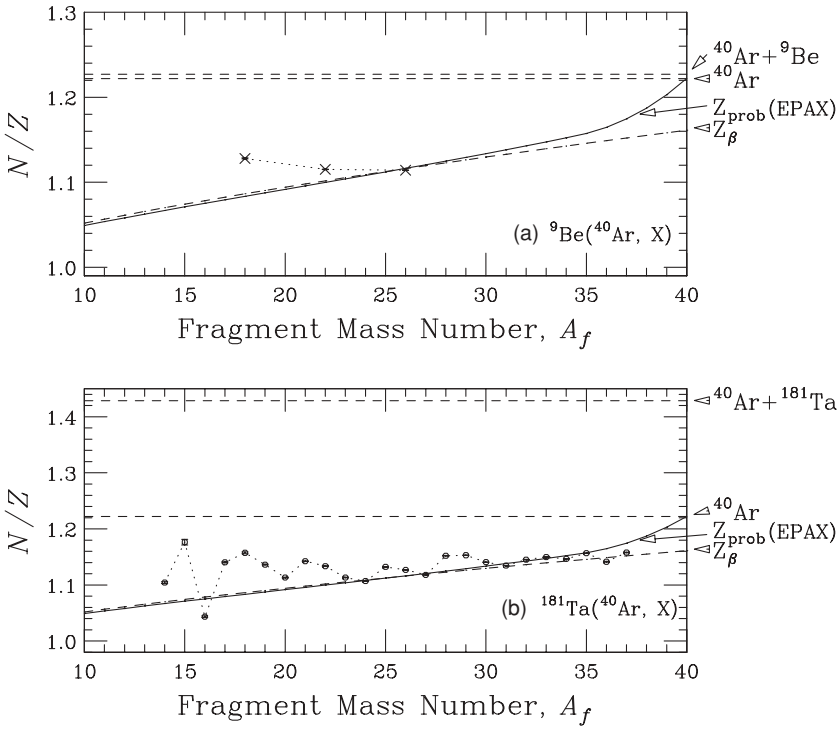

FIG. 17. Peak of charge distributions as a function of fragment mass for the production targets of (a) Be and (b) Ta. The solid curves are the most probable charge $Z_{\rm prob}$ of EPAX. The dashed curves are the β-stable charge Z_β. The dashed lines are the N/Z ratio of ^{40}Ar projectile and compounds of $^{40}\mathrm{Ar} + {}^{9}\mathrm{Be}$ and $^{40}\mathrm{Ar} + {}^{181}\mathrm{Ta}$, respectively.

was observed about 0.3 mass units toward the neutron-rich side. However, their result is different from our data. The fitting results of our charge distributions have shown no significant difference of $Z_{\rm prob}$ (EXP) between the Be and Ta targets.

We have already found that the factorization assumption is invalid for production of neutron-rich nuclei. The flexibility of the charge distribution except for the most probable charge is the slope parameter. Thus, we would seek the origin of target dependence in the slope constant U. Because of the BOF, U may change from a simple constant to a complex parameter that depends on target nuclei.

Since the target dependence of $Z_{\rm prob}$ has not been found, we assume that $Z_{\rm prob}$ can be described as the EPAX formula for both of the targets. We make an attempt to fit the data with a function of charge distribution. Fitting parameters were U on the neutron-rich side and mass yield Y, and we tried to obtain the fragment mass dependence of U. The fitting procedure is performed for the data of each fragment mass group, where every 4 mass units are combined to avoid poor statistics.

Figure 18 shows the U parameters as functions of fragment mass for both targets. We plot the values with the systematic errors. The slope parameter U of EPAX is a constant of 1.65 (dashed lines). The average of U is 1.62 for the Ta target. Smaller U gives larger values of production cross sections for neutron-rich nuclei. However, the U parameter of Be target is larger than 1.65 and shows fragment mass dependence. Our data demonstrate that the BOF is related to the target dependence of the U parameter for very neutron rich nuclei.

2. *Predictive power of new parametrization*

We have obtained the modified EPAX formula for the nuclear fragmentation at an intermediate energy for both Be and Ta targets. To illustrate the validity of our parametrization, we show an example of the production cross section predicted for extremely neutron rich nuclei. Figure 19 shows the predictive power of the new parametrization. The dashed and solid curves are the charge distribution of mass-24 isobars produced in the $^{40}\mathrm{Ar} + {}^{9}\mathrm{Be}$ and $^{40}\mathrm{Ar} + {}^{181}\mathrm{Ta}$ reactions, respectively. The solid box is the cross section of the fragmentation channel for

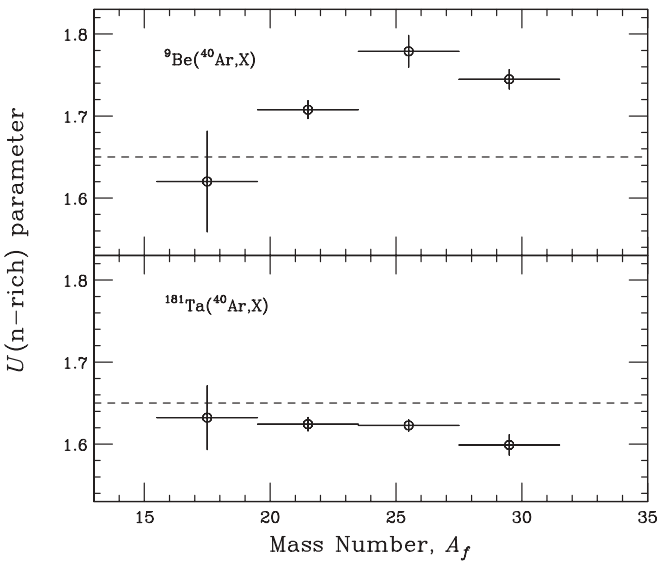

FIG. 18. U parameters as a function of fragment mass for the production targets of Be and Ta. On the assumption that the value of U is the same for every group of four sets of A_f data, the fitting results are shown with the systematic error. The dashed lines are the values of $U = 1.65$ from the EPAX.

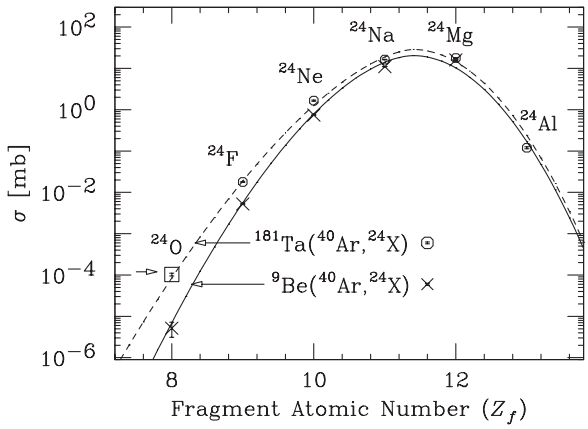

FIG. 19. Predictive power of cross sections of the new parametrization. The solid box marks the data of ^{24}O with a tantalum target.

^{181}Ta(^{40}Ar,^{24}O). This value acquired in another experiment [46] is clearly in agreement with our new parametrization.

G. Origin of BOF

We have studied the nuclear fragmentation reaction in nucleus-nucleus collisions at intermediate energies. The charge distributions of fragment cross sections acquired with the Be and Ta targets have revealed the BOF for very neutron rich nuclei. As for the origin of the BOF, we suggest two possible mechanisms that are responsible for the deviation in the charge distributions of pre-fragments during the reaction process of nuclear fragmentation.

One possible mechanism is the nucleon-exchange process. We observed the nucleon-exchange process in our data by identification of ^{36}Al, ^{37,38}Si, ^{38,39}P, and $^{37–40}$K, which have neutron or proton numbers larger than the projectile. Since the Ta target nucleus is richer in neutrons than Be, the probability of neutron transfer should be large. Recent research on very neutron rich products demonstrates the significant role of the target N/Z at the low-energy regime of $\sim$25A MeV [47,48]. The nucleon-exchange reaction between projectile and target nuclei during the abrasion process may break the factorization of fragment production cross sections.

The other mechanism is the isospin dependence of nucleon-nucleon scattering. The difference between proton-to-proton (σ_{pp}) and proton-to-neutron (σ_{pn}) scattering cross sections may lead to the deviation of pre-fragment charge distributions. As is well known, σ_{np} is larger than σ_{nn} and σ_{pp} when the nucleon energy is less than 500 MeV. In the projectile fragmentation process, a neutron-rich target nucleus easily knocks out protons in the projectile nucleus, so that the production of neutron-rich pre-fragments is promoted.

The discussions so far are qualitative. However, they can provide several predictions. First, if the nucleon-exchange process is the only reason for the BOF, the probability of nucleon exchange becomes large at low energies. Nuclear fragmentation experiments with lower incident beam energies than ours may reveal a large BOF effect for very neutron rich nuclei. Second, if the difference of the N-N reaction cross sections causes the BOF, nuclear fragmentation experiments with 100–800A-MeV beams should be carried out to confirm the BOF for very neutron rich nuclei. Since the cross section curves of σ_{pp} (σ_{pp}) and σ_{pn} intersect at 500 MeV, the difference in the U parameter between the Be and Ta targets might change sign. Further investigations of fragmentation cross sections around 500A MeV are of great interest.

V. SUMMARY AND CONCLUSION

Projectile fragmentation reactions at intermediate energies have been investigated using a 90–94A MeV ^{40}Ar beam at RIKEN-RIPS. We paid special attention to the target dependence. Measurement of longitudinal momentum distributions of projectile-like fragments within a wide range for fragment mass and charge including very neutron rich nuclei has been performed with ^{9}Be and ^{181}Ta targets.

By measuring the fragment momentum distribution, we revealed the reaction mechanisms at intermediate energies. First, a parabolic mass dependence of the momentum peak shift was observed in the data of both targets, and the high-momentum side widths are in good agreement with the Goldhaber model. These results show that the projectile fragmentation reaction is dominant. Second, fragment acceleration was observed together with the LE component in the Be-target data. The post-acceleration of the light fragments is interpreted as the response of the projectile spectator to the participant blast. The LE component is related to the multifragmentation process where the source is a highly excited compound system generated via central collision. Finally, a linear dependence of the low-momentum tail as a function of removed nucleons was found for both targets, and we identified ^{36}Al, ^{37,38}Si, ^{38,39}P, and $^{37–40}$K, which have neutron or proton numbers larger than the projectile. These results imply that the nucleons are exchanged between the projectile and target nuclei during the reaction process. Our conclusion is that we observed projectile fragmentation, multifragmentation, and transfer-like fragmentation.

We observed large target dependence of the cross sections to produce very neutron rich nuclei with $Z_\beta - Z_f \geqslant 2$. The deviation shows that the production cross sections of very neutron rich nuclei far from the stability line do not factorize. We suggested the nucleon exchange process and the isospin dependence of N-N scattering for the origin of BOF; however, the discussions so far are qualitative. Future experiments are needed to examine the target dependence of the cross sections at higher and lower energies to further elucidate this hypothesis.

ACKNOWLEDGMENTS

The authors wish to thank the RIKEN Ring Cyclotron staff and crew for their cooperation. We are also indebted to A. G. Artukh, G. A. Souliotis, and T. Shimoda for stimulating discussions. One of the authors (M.N.) acknowledges the financial support of the RIKEN Special Researchers' Basic Science Program.

[1] J. A. Winger *et al*., Nucl. Instrum. Methods B **70**, 380 (1992).
[2] N. Iwasa *et al*., Nucl. Instrum. Methods B **126**, 284 (1997); Th. Schwab, GSI Report No. 91-10, 1991 (unpublished).
[3] K. Sümmerer and B. Blank, Phys. Rev. C **61**, 034607 (2000).
[4] H. Sakurai *et al*., Phys. Lett. **B448**, 180 (1999).
[5] H. Sakurai *et al*., Phys. Rev. C **54**, R2802 (1996).
[6] M. Notani *et al*., Phys. Lett. **B542**, 49 (2002).
[7] H. Sakurai *et al*., Nucl. Phys. **A616**, 311 (1997).
[8] J. J. Gaimard and K. H. Schmidt, Nucl. Phys. **A531**, 709 (1991).
[9] J. R. Cummings *et al*., Phys. Rev. C **42**, 2530 (1990).
[10] D. Guillemaud-Müeller *et al*., Phys. Rev. C **41**, 937 (1990).
[11] H. H. Heckman *et al*., Phys. Rev. Lett. **28**, 926 (1972).
[12] A. S. Goldhaber, Phys. Lett. **B53**, 244 (1974).
[13] L. Tassan-Got *et al*., Nucl. Phys. **A524**, 121 (1991).
[14] T. Kubo *et al*., Nucl. Instrum. Methods Phys. Res. B **70**, 309 (1992).
[15] H. Kumagai *et al*., Nucl. Instrum. Methods Phys. Res. A **470**, 562 (2001).
[16] B. Robinet *et al*., Nucl. Instrum. Methods **190**, 197 (1981).
[17] R. Pfaff *et al*., Phys. Rev. C **51**, 1348 (1995).
[18] D. Bazin *et al*., Nucl. Phys. **A515**, 349 (1990).
[19] Ch. O. Bacri *et al*., Nucl. Phys. **A555**, 477 (1993).
[20] K. Van Bibber *et al*., Phys. Rev. Lett. **43**, 840 (1979).
[21] R. Dayras *et al*., Nucl. Phys. **A460**, 299 (1986).
[22] J. P. Dufour *et al*., Nucl. Instrum. Methods Phys. Res. A **248**, 267 (1986).
[23] T. Enqvist *et al*., Nucl. Phys. **A658**, 47 (1999).
[24] D. E. Greiner *et al*., Phys. Rev. Lett. **35**, 152 (1975).
[25] J. B. Cumming, Phys. Rev. Lett. **44**, 17 (1980).
[26] J. B. Cumming, P. E. Haustein, and H. C. Hseuh, Phys. Rev. C **24**, 2162 (1981).
[27] S. B. Kaufman *et al*., Phys. Rev. C **26**, 2694 (1982).
[28] D. J. Morrissey, Phys. Rev. C **39**, 460 (1989).
[29] V. Borrel *et al*., Z. Phys. A **314**, 191 (1983).
[30] V. Borrel *et al*., Z. Phys. A **324**, 205 (1986).
[31] L. Shi, P. Danielewicz, and R. Lacey, Phys. Rev. C **64**, 034601 (2001).
[32] J. Benlliure *et al*., Nucl. Phys. **A734**, 609 (2004).
[33] D. Guerreau *et al*., Nucl. Phys. **A447**, 37 (1985).
[34] M. C. Mermaz *et al*., Z. Phys. A **324**, 217 (1986).
[35] A. G. Artukh *et al*., Nucl. Instrum. Methods Phys. Res. A **426**, 605 (1999).
[36] G. Bizard *et al*., Phys. Lett. **B172**, 301 (1986).
[37] D. J. Olson *et al*., Phys. Rev. C **28**, 1602 (1983).
[38] K. Sümmerer *et al*., Phys. Rev. C **42**, 2546 (1990).
[39] R. Silberberg and C. H. Tsao, Astrophys. J. Suppl. **25**, 315 (1973).
[40] R. Silberberg *et al*., Astrophys. J. Suppl. **58**, 873 (1985).
[41] S. Kox *et al*., Phys. Rev. C **35**, 1678 (1987).
[42] M. Buenerd *et al*., Nucl. Phys. **A424**, 313 (1984).
[43] J. Galin *et al*., Z. Phys. A **278**, 347 (1976).
[44] M. Lefort and Ch. Ngô, Ann. Phys. (Paris) **3**, 5 (1978).
[45] D. Guerreau *et al*., Phys. Lett. **B131**, 293 (1983).
[46] Y. Yanagisawa *et al*., Phys. Lett. **B566**, 84 (2003).
[47] G. A. Souliotis *et al*., Phys. Rev. Lett. **91**, 022701 (2003).
[48] G. A. Souliotis *et al*., Phys. Lett. **B588**, 35 (2004).